How Nested Bars Enhance, Modulate, and Are Destroyed by Gas Inflows

Zhi Li[1,2,3] , Min Du[4] , Victor P. Debattista[5] , Juntai Shen[2,6] , Hui Li[7,8] , Jie Liu[9] , Mark Vogelsberger[10] ,
Angus Beane[11] , Federico Marinacci[12] , and Laura V. Sales[13]

[1] Shanghai Key Lab for Astrophysics, Shanghai Normal University, 100 Guilin Road, Shanghai 200234, People's Republic of China
[2] Department of Astronomy, School of Physics and Astronomy, Shanghai Jiao Tong University, 800 Dongchuan Road, Shanghai 200240, People's Republic of China;
jtshen@sjtu.edu.cn
[3] Tsung-Dao Lee Institute, Shanghai Jiao Tong University, Shanghai 200240, People's Republic of China
[4] Department of Astronomy, Xiamen University, Xiamen, Fujian 361005, People's Republic of China; dumin@xmu.edu.cn
[5] Jeremiah Horrocks Institute, University of Central Lancashire, Preston PR1 2HE, UK
[6] Key Laboratory for Particle Astrophysics and Cosmology (MOE)/Shanghai Key Laboratory for Particle Physics and Cosmology, Shanghai 200240, People's
Republic of China
[7] Department of Astronomy, Tsinghua University, Beijing 100084, People's Republic of China
[8] Department of Astronomy, Columbia University, New York, NY 10027, USA
[9] Shanghai Astronomical Observatory, Chinese Academy of Science, 80 Nandan Road, Shanghai, 200030, People's Republic of China
[10] Department of Physics & Kavli Institute for Astrophysics and Space Research, Massachusetts Institute of Technology, Cambridge, MA 02139, USA
[11] Center for Astrophysics | Harvard & Smithsonian, Cambridge, MA, USA
[12] Department of Physics & Astronomy "Augusto Righi", University of Bologna, via Gobetti 93/2, I-40129 Bologna, Italy
[13] Department of Physics and Astronomy, University of California, Riverside, CA 92521, USA

Abstract

Gas flows in the presence of two independently rotating nested bars remain not fully understood but are likely to play an important role in fueling the central black hole. We use high-resolution hydrodynamical simulations with detailed models of subgrid physics to study this problem. Our results show that the inner bar in double-barred galaxies can help drive gas flow from the nuclear ring to the center. In contrast, gas inflow usually stalls at the nuclear ring in single-barred galaxies. The inner bar causes a quasiperiodic inflow with a frequency determined by the difference between the two bar pattern speeds. We find that the star formation rate is higher in the model with two bars than in that with one bar. The inner bar in our model gradually weakens and dissolves due to gas inflow over a few billion years. Star formation produces metal-rich/α-poor stars, which slows the weakening of the inner bar but does not halt its eventual decay. We also present a qualitative comparison of the gas morphology and kinematics in our simulations with those of observed double-barred galaxies.

Unified Astronomy Thesaurus concepts: Barred spiral galaxies (136); Interstellar medium (847); Hydrodynamical simulations (767); Galaxy evolution (594); Stellar feedback (1602); Active galactic nuclei (16); Galaxy nuclei (609)

1. Introduction

Galaxies with two nested stellar bars are termed "double-barred galaxies" (S2Bs; see Laine et al. 2002; Erwin 2004; Shlosman 2005; Buta et al. 2015). About 20% of disk galaxies appear to be S2Bs (Laine et al. 2002; Erwin 2011). In such systems, the two bars are observed to be randomly oriented with respect to each other (Buta & Crocker 1993; Friedli & Martinet 1993), implying two independent rotation speeds that are consistent with theoretical expectations (e.g., Maciejewski & Sparke 2000; Debattista & Shen 2007; Du et al. 2015). The inner bars in S2Bs are also dubbed "nuclear" or "secondary" bars in some works. These terms may be less appropriate, since observations have shown that inner bars can be as large as some short single bars (semimajor axes of 2–3 kpc; see Erwin 2005; de Lorenzo-Cáceres et al. 2020). Recent studies have suggested that inner bars are probably scaled-down replicas of outer bars based on resolved spatial maps of the mean stellar population properties (de Lorenzo-Cáceres et al. 2019b; Méndez-Abreu et al. 2019; Bittner et al. 2021).

The gas inflow driven by the large-scale bar generally stalls at a starburst nuclear ring with a typical size of a few hundred parsecs, preventing accretion onto the supermassive black hole (SMBH; e.g., Fanali et al. 2015; Li et al. 2017; Tress et al. 2020). Inner bars have been hypothesized to be an important mechanism for further removing gas angular momentum, in a manner similar to their large-scale counterparts (e.g., Shlosman et al. 1989; Friedli & Martinet 1993). The inflowing gas driven by the inner bar may be a possible mechanism to contribute to the growth of the SMBH in the galactic center. However, the fuel may be choked off as the inner bar gradually dissolves for a short time (~1 Gyr) when the SMBH becomes massive enough (~0.1% stellar mass of the host galaxy; Du et al. 2017; Nakatsuno & Baba 2023), and the growth is therefore self-limiting. The remnant of the destroyed inner bar leads to the formation of a spheroidal component that is similar to a small classical bulge (Guo et al. 2020). Interestingly, observations have found that local S2Bs are likely to host classical instead of pseudobulges (de Lorenzo-Cáceres et al. 2019a), although it would be difficult to determine the origin of these classical bulges.

One important assumption in the above scenario is that inner bars promote gas inflows from the nuclear ring to the center. This has long been speculated to be the case (e.g., Shlosman et al. 1989; Heller et al. 2007; Namekata et al. 2009; Hopkins

& Quataert 2010), but studies have provided conflicting results (e.g., Maciejewski et al. 2002; Rautiainen et al. 2002). For example, the "bars-within-bars" model of Shlosman et al. (1989) and Hopkins & Quataert (2010) supports the idea that inner bars (or small-scale bars) can reduce gas angular momentum just like large-scale bars; however, some theoretical studies of gas motions in S2B potentials have argued that the gas flow patterns differ fundamentally between single and nested bars, and the inner bar cannot enhance the central mass inflow rate due to the lack of shocks (Maciejewski et al. 2002; Rautiainen et al. 2002; Shlosman & Heller 2002).

Nevertheless, there are still large uncertainties/simplifications in the modeling of nested bars that can affect the gas behaviors. For instance, the two bars in the S2B simulations of Maciejewski et al. (2002) and Namekata et al. (2009) are modeled as rigid (Ferrers) ellipses whose torque distributions are different from those of real bars (Buta & Block 2001; Li et al. 2017). In addition, both the pattern speeds and the shapes of the bars are pulsating in a self-consistent, dynamically decoupled double-barred system (e.g., Shen & Debattista 2009; Du et al. 2015; Wu et al. 2016), and this effect on gas flows has been less explored in the literature. Moreover, star formation and feedback in the central kiloparsec may also affect the inner bar dynamics, including the gas inflow (Wozniak 2015), and this requires detailed modeling of subgrid physics, as well as sufficient numerical resolution. It remains an important question, therefore, whether inner bars are able to drive gas inflows and potentially activate the central SMBH, which motivates us to perform an in-depth numerical study of gas flows in S2Bs with state-of-the-art subgrid physics implemented. We would like to investigate (1) whether the inner bar can drive gas further to the center using a realistic S2B model that qualitatively matches the observed stellar kinematics, (2) how the gas flows respond to a pulsating inner bar, and (3) how different the gas flow pattern is between single- and double-barred galaxies, especially in the central region.

The paper is organized as follows. Section 2 describes our simulation setups. Section 3 presents the evolution of our S2B models using different gas prescriptions and isolates the effects of the inner bar with control models. Section 4 compares the properties of our simulated S2Bs with observations. We discuss the implications and limits of this study in Section 5. Section 6 gives a summary of our results.

2. Simulations

The fiducial S2B model of Du et al. (2017) nicely reproduces many observed features in real S2B galaxies, such as σ-humps/hollows and h_4 rings (see Du et al. 2016; de Lorenzo-Cáceres et al. 2019b). The long-lived inner bar in this model forms spontaneously from a cool inner disk via dynamical instabilities. For our study, we choose to adopt a similar setup, as detailed below. We select the snapshot corresponding to the time $t = 2.7$ Gyr of the fiducial model in Du et al. (2017) as the initial condition for the stars in our simulations. At this time, the semimajor axis of the inner bar is ~ 0.75 kpc, while the outer bar has a semimajor axis of ~ 7.5 kpc. The inner bar rotates roughly three times as fast as its outer counterpart. The two bars have reached a relatively steady state, but the pattern speeds of the two bars are not stationary, and the shape of the bars also changes; i.e., the bars are pulsating during the evolution (see also Debattista & Shen 2007). The stellar disk in our model has a mass of $6.0 \times 10^{10} M_\odot$. We use the same
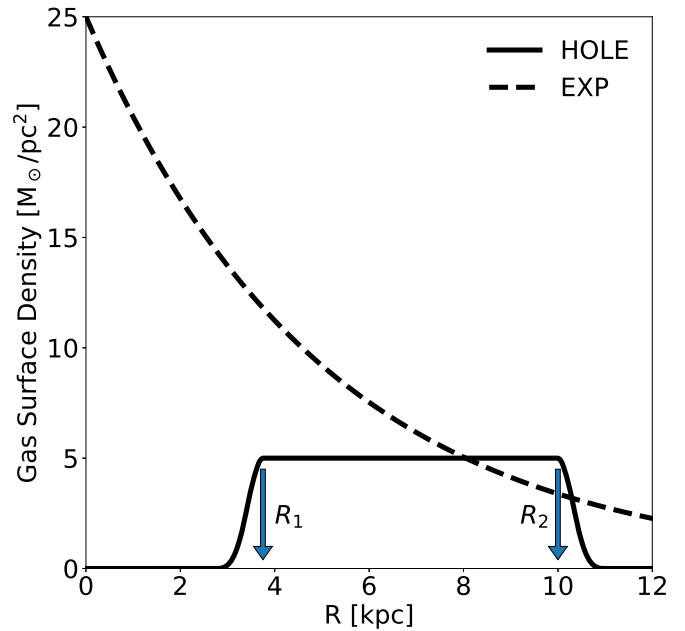

Figure 1. Initial gas surface density profiles used in our models. The solid curve shows the HOLE profile, with the two arrows denoting the inner and outer boundaries at $R_1 = 3.75$ and $R_2 = 10.0$ kpc; the dashed line shows the EXP profile with a central density $\Sigma_0 = 25 M_\odot \, \mathrm{pc}^{-2}$ and scale radius $R_d = 5$ kpc.

logarithmic rigid dark matter halo that Du et al. (2015, 2017) used, which has a potential given by $\Phi(r) = 0.5 V_h^2 \ln(r^2 + r_h^2)$, with $V_h = 157.4 \, \mathrm{km \, s}^{-1}$ and $r_h = 37.5$ kpc, where r is the spherical radius with respect to the galactic center. This rigid halo simplifies our simulation, while the dynamics at the center, where the baryonic components dominate, are barely changed. We refer the reader to Du et al. (2015, 2017) for further details of the model.

We insert a lightweight gas disk into this snapshot to study gas flows under the live S2B potential. We start the simulation time from when we insert the gas disk. There are two different gas surface density profiles at $t = 0$ used in our models, as shown in Figure 1; one is set to an annulus with inner and outer radii at $R_1 = 3.75$ and $R_2 = 10.0$ kpc, respectively, where R is the cylindrical radius with respect to the galactic center (labeled as "HOLE"). Here R_1 is chosen to be close to the middle of the outer bar. This annulus configuration aims to protect the inner bar from the rapid formation of a gaseous central massive concentration (CMC) that may dissolve the inner bar quickly (e.g., Wozniak 2015; Du et al. 2017; Guo et al. 2020; Nakatsuno & Baba 2023). The initial inner boundary R_1 also helps us focus on the inflowed gas during the evolution of the model. The surface density of the annulus gas disk between R_1 and R_2 is uniform[14] with $\Sigma_{\mathrm{gas}} = 5 M_\odot \, \mathrm{pc}^{-2}$ and is tapered off by a cubic spline function with a characteristic width of 0.2 kpc outside R_1 and R_2 (see also a similar initial gas disk setup in Beane et al. 2023). The total gas mass is therefore $1.5 \times 10^9 M_\odot$; the other is set to have an exponential surface density profile (labeled as "EXP"). The scale radius of the exponential gas disk is $R_d = 5$ kpc, and the central gas surface density is $\Sigma_0 = 25 M_\odot \, \mathrm{pc}^{-2}$. The total gas mass is therefore

---

[14] A uniform gas disk is commonly used in studying bar-driven gas flows because it results in no pressure gradient in the radial direction (e.g., Athanassoula 1992; Englmaier & Gerhard 1997; Kim et al. 2012; Sormani et al. 2015).

Table 1
Model Setup

Model (1)	γ (2)	Gas Self-gravity (3)	SMUGGLE (4)	Gas Profile (5)	Gas Fraction (6)	Galaxy Type (7)
S2BISO	1.0	Off	Off	HOLE	2.5%	S2B
S2BSMU	5/3	On	On	HOLE	2.5%	S2B
S1BSMU	5/3	On	On	HOLE	2.5%	SB
S0BSMU	5/3	On	On	HOLE	2.5%	SA
S2BEXP	5/3	On	On	EXP	6.5%	S2B

Note. List of models in this work. Column (1): model name. Column (2): adiabatic index γ, where $\gamma = 1$ corresponds to the isothermal EoS, while $\gamma = 5/3$ is for ideal monoatomic gas. Column (3): switch for gas self-gravity. Column (4): switch for SMUGGLE model. Column (5): initial surface density profile of the gas disk, where HOLE means an initial uniform gas disk with an inner boundary of $R_1 = 3.75$ kpc and outer boundary of $R_2 = 10.0$ kpc, while EXP means an initial exponential gas disk without the inner boundary (see also Figure 1). Column (6): gas mass fraction relative to the stellar disk. Column (7): galaxy morphology of the model.

$3.9 \times 10^9 \, M_\odot$. Although this gas disk changes both the gas surface density profile and the gas mass at the same time, it primarily tests the effects of a massive CMC on the bars in a relatively extreme case. The vertical density profile is chosen to be in hydrostatic equilibrium following Springel et al. (2005) and Wang et al. (2010) for both gas disk types. We start the gas disk on circular orbits obtained from the axisymmetrized galactic potential. The initial temperature of the gas disk is set to 1.5×10^4 K. All gas cells at $t = 0$ have solar metallicity and alpha-elements as described in Asplund et al. (2009).

Gas cooling and heating, star formation, and stellar feedback are included via the interstellar medium (ISM) and the stellar feedback model Stars and MUltiphase Gas in GaLaxieEs (SMUGGLE; Marinacci et al. 2019). This model reproduces well the observed feedback-regulated star formation and has been widely used for studying galaxy formation and evolution (e.g., Burger et al. 2022; Li et al. 2022; Sivasankaran et al. 2022; Tacchella et al. 2022). We adopt a local star formation efficiency of $\epsilon_{sf} = 0.01$ and a star formation density threshold of $\rho_{th} = 100 \, \text{cm}^{-3}$ in SMUGGLE. We use the same stellar yields and evolution model as the original Illustris simulation (Vogelsberger et al. 2013).

The simulations are performed using the moving-mesh code AREPO (Springel 2010; Weinberger et al. 2020). The simulation box size is 60 kpc, so the boundary effects on the gas disk are negligible. There are 3.8 million stellar particles with a fixed softening length of 25 pc and 1.3 million initial gas cells with adaptive softening enabled. The minimum adaptive softening is set to 0.25 pc, and the target mass of the gas cells is $\approx 1100 \, M_\odot$. The galaxy properties modeled with SMUGGLE nicely converge at this resolution (Marinacci et al. 2019). The minimum gas cell radius in our simulations reaches ~0.14 pc.

We present five models with configurations summarized in Table 1. The fiducial S2B model is referred to as S2BSMU, with SMUGGLE enabled. Model S2BISO has the same initial conditions as S2BSMU but uses the isothermal equation of state (EoS) and excludes gas self-gravity to avoid gravothermal catastrophe. The effective sound speed in S2BISO is $c_s \approx 10 \, \text{km s}^{-1}$ (obtained from the initial gas temperature). This sound speed reflects the average velocity dispersion between molecular clouds rather than the microscopic

temperature of the diffuse gas. We further run two additional control models (S1BSMU and S0BSMU) to highlight the gravitational effects of bars. We generate S1BSMU by azimuthally scrambling[15] the stellar particles at $R \leqslant 0.75$ kpc of S2BSMU in the initial condition. Model S1BSMU is thus a single-barred (SB) galaxy whose bar structure is almost the same as the outer bar of S2BSMU. Similarly, we generate S0BSMU by scrambling stellar particles at $R \leqslant 7.5$ kpc, thus producing an unbarred galaxy. These four models have the exact same azimuthally averaged mass profile and rotation curve at $t = 0$. The gas mass fraction relative to the stellar disk in these four models is 2.5%, and the models are run for ~1.9 Gyr. Model S2BEXP has nearly identical initial conditions as S2BSMU, with the exception of an initial exponential rather than uniform gas disk. Consequently, the gas mass fraction is increased to 6.5%; this model is run for ~3.8 Gyr.

3. Results

3.1. Comparing the S2B Model with Different Gas Assumptions

In this subsection, we show how stellar feedback affects the gas morphology, as well as the mass inflow rate in the same S2B potential, by comparing the fully star-forming model S2BSMU with the isothermal model S2BISO.

3.1.1. Gas Morphology in the Inner and Outer Regions

We first present gas flow patterns in S2BISO with the isothermal EoS. This EoS assumes that the specific internal energy of the ISM is the result of a balance between heating and cooling and can be regarded as a first-order approximation of the observed cold gas in galactic disks. Although it is a simplification of the true multiphase nature of the ISM, previous studies have shown that the isothermal EoS reproduces the observed gas dynamics in bars reasonably well (e.g., Weiner et al. 2001; Lin et al. 2013; Fragkoudi et al. 2017). We therefore start with this simple model to highlight the gravitational effects of bars. It also helps us to better compare our model with previous S2B simulations that use the isothermal EoS (e.g., Maciejewski et al. 2002; Shlosman & Heller 2002; Namekata et al. 2009).

Figure 2 plots the surface density of the stellar (top) and gas (bottom) disk in S2BISO at four different times. The models are rotated such that the outer bar is always aligned with the x-axis for easier comparison. The two stellar bars are clearly outlined by the white contours of stellar surface density. Note that the inner bar has different orientations with respect to the outer bar due to its different (higher) pattern speed. The first two columns show the earlier evolution of the model. The initial circular and uniform gas disk is gradually distorted by the bars, forming a pair of strong shocks at the leading side of the outer bar, together with a two-arm spiral around 10 kpc. Gas flows inward to the inner boundary soon after the simulation starts (first column), then accumulates at a high-density nuclear ring with a size of ~1.5 kpc (second column). The inner bar lies within the gaseous nuclear ring, as seen also in observations (Buta et al. 2015). Overall, the large-scale flow pattern at $R \gtrsim 4$ kpc resembles the results of previous SB

---

[15] Scrambling means that the in-plane position (x, y) and velocity (v_x, v_y) of each stellar particle are rotated by a random angle ϕ with respect to the galactic center. Here ϕ follows a uniform distribution on the interval $[0, 2\pi)$ (see also Brown et al. 2013; Li et al. 2014).
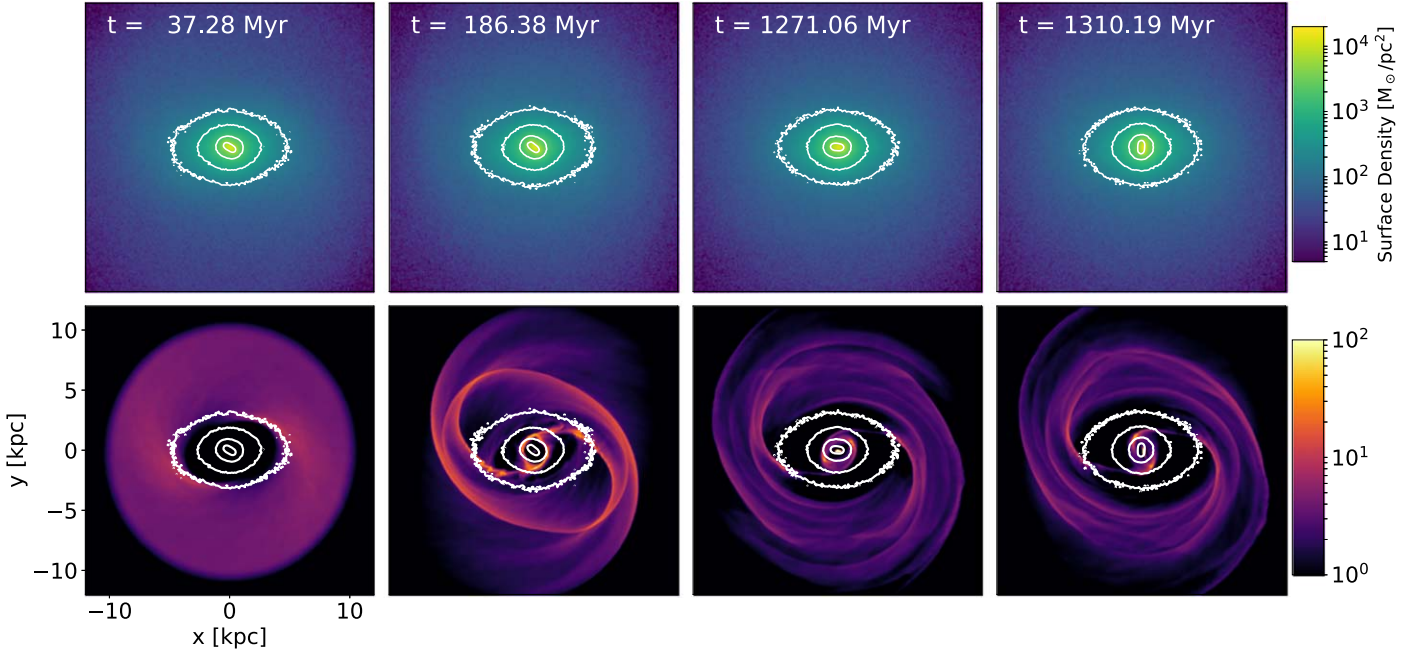
Figure 2. Evolution of model S2BISO. Top: stellar surface density. Bottom: gas surface density. White lines represent the contours of the stellar surface density placed at 0.16, 0.54, 1.85, and $6.31 \times 10^3 \, M_\odot \, pc^{-2}$. The two stellar bars are clearly outlined by the contours. The first two columns show the early evolution when the two bars are misaligned, while they are parallel in the third column and perpendicular in the fourth column. The evolution time is given at the top. The disk rotates counterclockwise.
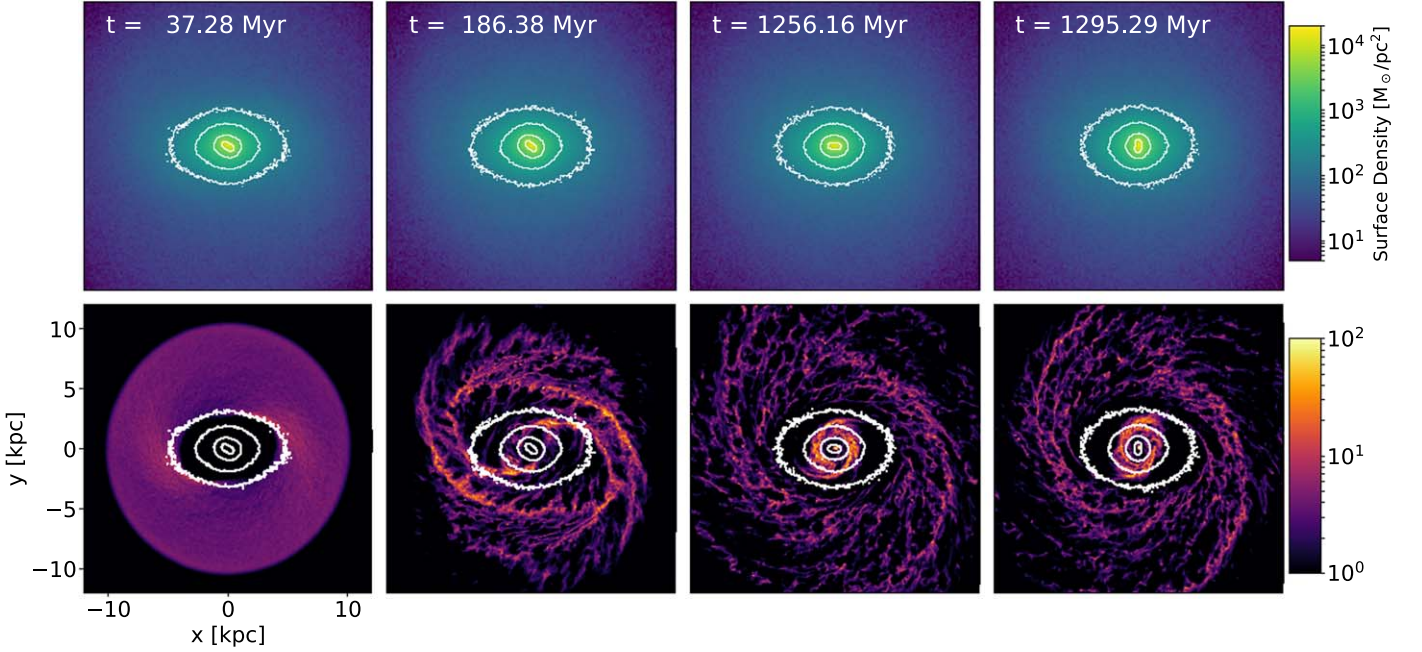
Figure 3. Similar to Figure 2 but for S2BSMU.

simulations (e.g., Kim et al. 2012; Li et al. 2015; Sormani et al. 2015). The morphology and kinematics of the gas in this region is mainly dominated by the outer bar potential and is not sensitive to the inner bar orientation, as shown in the third (parallel bars) and fourth (perpendicular bars) columns.

We next present S2BSMU, which resolves the multiphase gas with explicit star formation and stellar feedback included. When comparing the surface densities in Figure 3 with those in Figure 2, the stellar component is almost the same. The smooth gas features (e.g., the shocks, spirals, and nuclear ring) in S2BISO become more flocculent and clumpy in S2BSMU due

to local stellar feedback, but their overall shapes remain mostly unchanged. This is expected, since the gas mass fraction is only 2.5% in our models. The global star formation rate (SFR) is around 0.1–$0.2 \, M_\odot \, yr^{-1}$ during the entire simulation, so the gas evolution on a large scale is still governed by the nonaxisymmetric stellar potential.

The major differences between S2BISO and S2BSMU emerge in the central $R \lesssim 2 \, kpc$, which is shown in Figure 4. In this figure, we present gas surface densities in four snapshots with different bar orientations indicated by the red (outer bar) and blue (inner bar) sticks in the bottom right corner of each
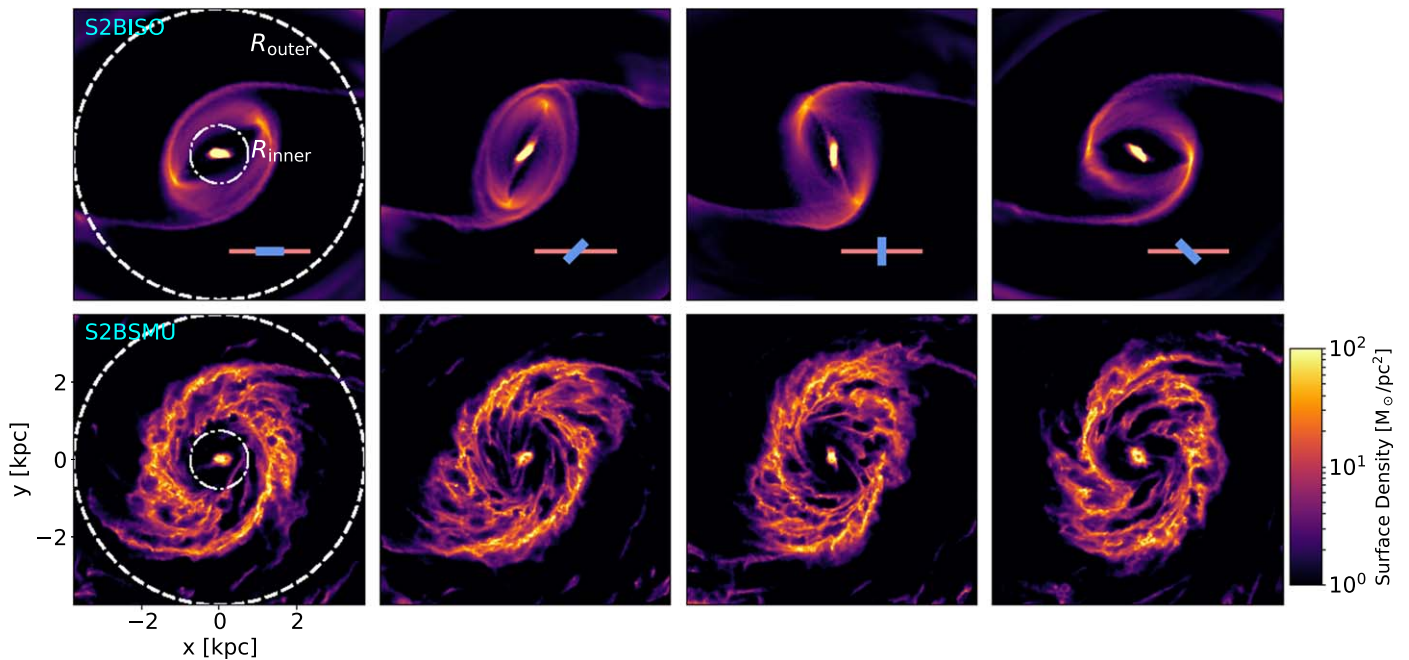
Figure 4. Comparison of the inner gas surface density between S2BISO (top) and S2BSMU (bottom). The columns represent four different epochs when the two bars have different angles with respect to each other (indicated by the red and blue sticks in the bottom right corner of each panel in the top row). The snapshots are taken at $t = 1.271$, 1.287, 1.310, and 1.334 Gyr for S2BISO and $t = 1.256$, 1.272, 1.295, and 1.317 Gyr for S2BSMU. The dashed and dotted–dashed circles denote two characteristic cylindrical radii of $R_{\mathrm{outer}} = 3.75$ and $R_{\mathrm{inner}} = 0.75$ kpc. The gas disk rotates counterclockwise.

panel in the top row. The shape of the nuclear ring in S2BISO clearly depends on the relative orientations between the two bars; it tends to be more elliptical when the bars turn from parallel to perpendicular (second and third columns), and vice versa. Furthermore, the ring slightly leads the inner bar during the rotation. The cyclically changing shape of the nuclear ring is consistent with earlier S2B simulations and orbit analysis (Maciejewski & Sparke 2000; Laine et al. 2002). We also see straight shocks (which would be traced by dust lanes) at the edges of the inner bar (more obvious in the second and third columns) that can drive gas to the center. This flow pattern is different from those found by Maciejewski et al. (2002) and Shlosman & Heller (2002), and we discuss the possible reasons in Section 5.1. On the other hand, the ring in S2BSMU roughly maintains the same shape regardless of the bar's relative orientations. This can be understood in terms of a simple estimation of the value of the gas kinetic energy and the energy injected by stellar feedback; the gas in the ring has a typical rotation velocity of $\sim$200 km s^{-1}, and the gas mass of the ring is $\sim 2.0 \times 10^8 \, M_\odot$, which gives a kinetic energy of 8.0×10^{55} erg; the energy released by the supernova feedback in the ring during one ring rotation ($\sim$60 Myr) is $\approx$6–9 $\times 10^{55}$ erg. The two comparable energies suggest that feedback becomes as important as gravity in about one dynamical timescale, and the effect of the inner bar on the ring shape is therefore less prominent. We also find that a small gas bar is formed and corotates with the inner bar in S2BISO, but this structure seems to be erased by stellar feedback in S2BSMU.

3.1.2. Bar Amplitudes and Mass Inflow Rate

A more quantitative analysis of the evolution of the two S2B models is presented in Figure 5. The two columns display the properties of the isothermal (S2BISO) and multiphase (S2BSMU) models. We first compare the bar amplitude measured by the normalized Fourier component A_2/A_0 in the

first row. The bars in S2BISO are relatively stable, although the bar amplitudes pulsate as the inner bar rotates with respect to the outer one, which is also seen in previous simulations (Debattista & Shen 2007; Wozniak 2015; Du et al. 2015; Wu et al. 2016). On the other hand, the bar amplitudes exhibit a weakening trend in S2BSMU. This is because gas self-gravity is included in this model, and the accumulating gas forms a CMC that can weaken the bars (Athanassoula 2003; Shen & Sellwood 2004; Du et al. 2017). In the second row, we plot the enclosed gas mass at two characteristic radii ($R_{\mathrm{outer}} = R_1 = 3.75$ and $R_{\mathrm{inner}} = 0.75$ kpc), which can be seen by the white dashed and dotted–dashed circles in the first column of Figure 4. Here R_{outer} is equal to R_1, which corresponds to the inner boundary of the initial gas disk (see Section 2), and most of the gas inflow driven by the outer bar accumulates inside this radius; R_{inner} is approximately the size of the inner bar. We see that the enclosed mass quickly increases with time; it reaches $\sim 3.0 \times 10^8 \, M_\odot$ inside R_{outer} within 1 Gyr in both models. This value is about 20% of our initial gas disk mass and about 0.5% of the stellar disk mass. Note that the enclosed mass includes both gas and newly formed stars in S2BSMU. It is also worth noting that when the inner bar in S2BSMU starts to weaken at $t \gtrsim 1.3$ Gyr, the mass enclosed within R_{inner} reaches $\sim$0.1% of the disk mass. This is consistent with the inner bar dissolution criterion predicted in Du et al. (2017). The outer bar in this model is also weakened over time.

About 80% of the gas in the nuclear ring is accumulated inside R_{inner} in S2BISO, but the fraction drops to $\sim$30% in S2BSMU. There are probably two reasons for this. (1) Rapid star formation consumes gas in the nuclear ring at $R \sim 2$ kpc of S2BSMU, which makes less gas available for the inner bar to drive inward to R_{inner}. The gravitational dynamical timescale (i.e., freefall timescale) for a gas cell to form stars in the ring with a typical gas density of $0.5 \, M_\odot \, \mathrm{pc}^{-3}$ is around 10 Myr, while the gas rotation period in the ring is $\sim$60 Myr, and it
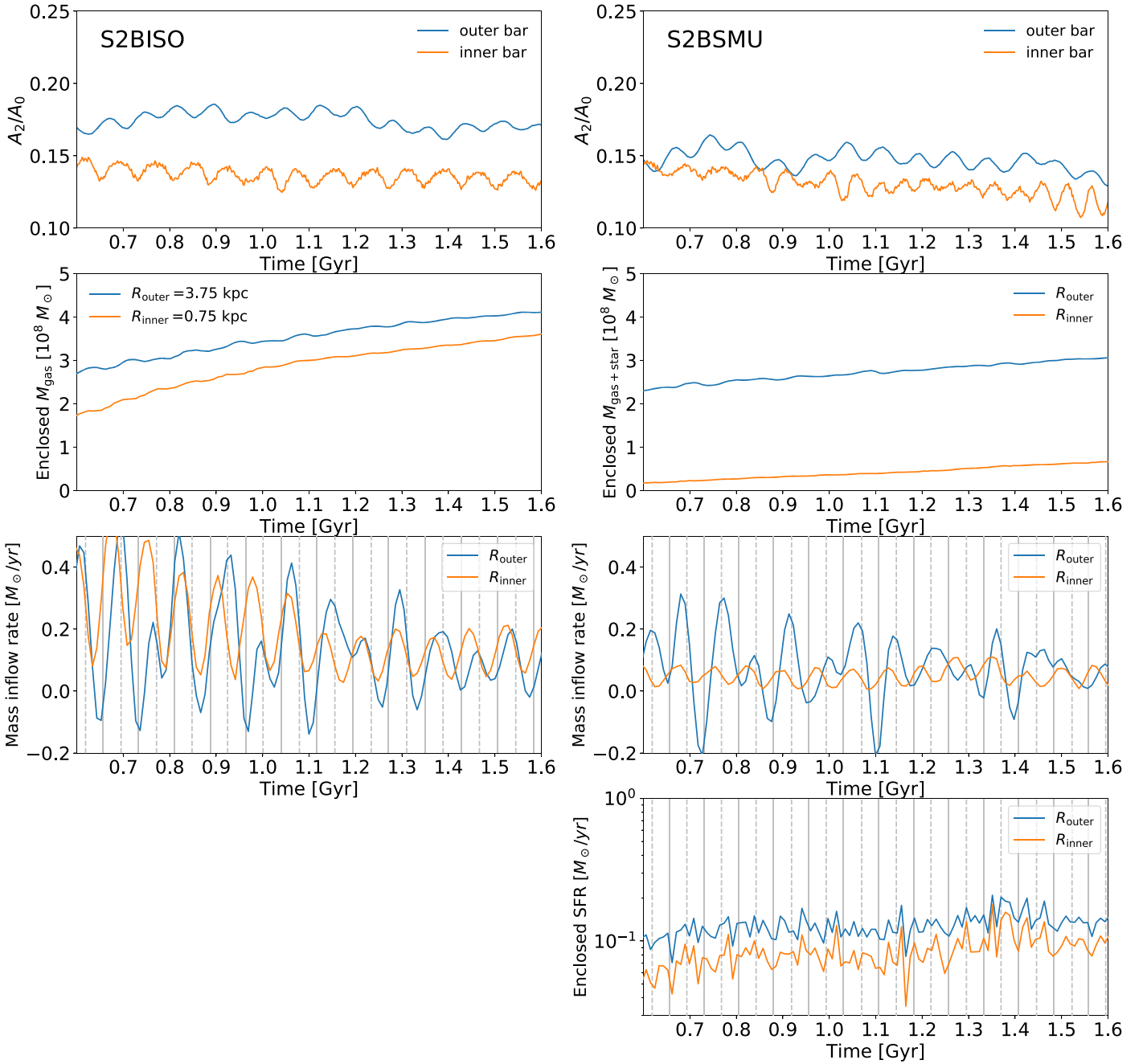
Figure 5. Bar properties and gas inflows in the S2BISO (left) and S2BSMU (right) models. First row: outer and inner bar amplitudes. The Fourier components A_2 and A_0 are measured in the radial range of 2.4–7.5 kpc for the outer bar and 0–0.75 kpc for the inner bar. Second row: enclosed mass of gas (S2BISO) and gas plus newly formed stars (S2BSMU) inside R_{inner} and R_{outer}. Third row: mass inflow rate obtained from the time derivative of the lines in the second row. Vertical gray solid and dashed lines indicate the moments when the two bars are aligned and perpendicular, respectively. Fourth row: enclosed SFR in S2BSMU. This quantity is calculated based on the total mass of new stars inside the given radius that are formed in the past 10 Myr.

usually takes a few rotation periods for the inner bar to remove gas angular momentum. Since the dynamical timescale is longer than the local star formation timescale, a large fraction of gas will form stars in the ring instead of being driven inward by the inner bar. By contrast, there is no mechanism to consume gas in S2BISO, and the inner bar can therefore drive most gas in the ring down to the center. (2) The ring in S2BISO is smaller in size and periodically changes its shape (Figure 4). This helps the gas in the ring to be more easily affected by the inner bar torque in S2BISO compared to S2BSMU.

The third row of Figure 5 shows the mass inflow rate at the two radii, obtained by taking the time derivative of the lines in

the second row. We focus on 0.6–1.6 Gyr, when the inner bars are relatively stable in both models. The mass inflow rates oscillate with time and seem to be quasiperiodic. We label the moments when the inner and outer bars are parallel (solid vertical lines) and perpendicular (dashed vertical lines) to each other. The inflow rate tends to peak when the bars are perpendicular, consistent with clearer shock features in the second and third panels in the top row of Figure 4. The oscillation period (~78 Myr) is therefore determined by the pattern speed difference (or beat frequency) of the two bars. This bar-modulated periodic gas inflow is also reported in some of the previous S2B simulations (Shlosman & Heller 2002;
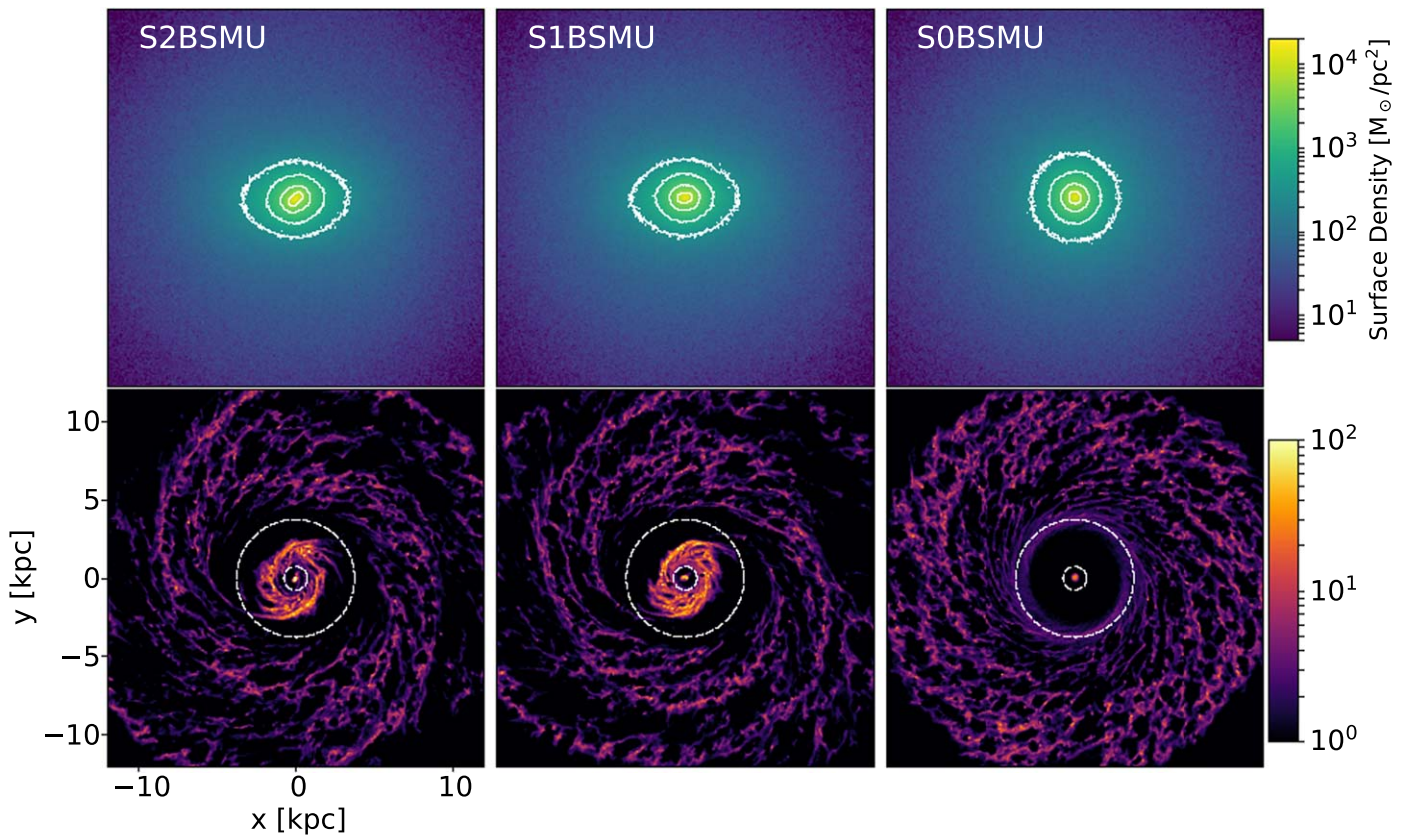
Figure 6. Stellar and gas surface density comparison using S2BSMU, S1BSMU, and S0BSMU at $t = 1.8$ Gyr, from left to right as labeled. The top row is the stellar surface density, and the bottom row is the gas surface density. The outer bar is aligned with the x-axis for S2BSMU and S1BSMU. The dashed circles in the bottom row denote the two characteristic cylindrical radii, $R_{\rm outer} = 3.75$ and $R_{\rm inner} = 0.75$ kpc.

Namekata et al. 2009), but here we show for the first time that the inflow is strongest when the two bars are perpendicular, possibly due to clearer shocks inside the inner bar at this angle. Interestingly, this trend remains in S2BSMU, although the spatial distribution of gas seems to be independent with respect to the bar orientations due to local stellar feedback (see the bottom row of Figure 4). This may suggest gravity still dominates the evolution of central gas inflows, similar to the case studied in Romeo & Fathi (2016). It is worth noting that there appears to be no regular pattern in the enclosed SFR curve of S2BSMU within $R_{\rm inner}$, despite the fact that the model has a nearly periodic gas supply in this region (but also see the results in Moon et al. 2022).

Figure 5 demonstrates that the inner bar does promote gas inflow to the center. However, the mass inflow rate at $R_{\rm inner}$ in S2BSMU is considerably lower than that in S2BISO. It is therefore natural to ask whether the amplitude of the central mass inflow rate is still dominated by the inner bar potential when stellar feedback is included.

3.2. Comparing the S2B Model with the SB and SA Models

In this subsection, we compare three models with different bar numbers but all with the SMUGGLE model (S2BSMU, S1BSMU, and S0BSMU) to isolate the effects of the inner bar on gas dynamics from (stochastic) stellar feedback.

3.2.1. Mass Inflow Rate and SFR

Figure 6 shows the stellar and gas surface densities of S2BSMU, S1BSMU, and S0BSMU at $t = 1.8$ Gyr. These three models have the same azimuthally averaged mass distribution at $t = 0$. Gas flow patterns in S2BSMU and S1BSMU are very similar outside $R \sim 1$ kpc; they both form a pair of spiral arms and a bright nuclear ring produced by the outer bar. Model S0BSMU only shows flocculent spirals, and little gas can flow into $R_{\rm outer}$, as no bar is present.[16] The gas distribution of this model looks similar to that of NGC 2775 (e.g., Leroy et al. 2021).

Inside $R \sim 1$ kpc, the gas behaves differently in S2BSMU and S1BSMU, as shown in Figure 7. The first two columns are zoom-in views of the stellar and gas surface densities in Figure 6. Inflow signatures can be spotted in S2BSMU, as multiple gas streams formed inside the nuclear ring down to the galactic center. On the other hand, the nuclear ring has a relatively well-defined inner boundary in S1BSMU, implying that the inflow has stalled at this radius. This is not surprising, since the nuclear ring in SB galaxies serves as a barrier that prevents gas from reaching the nucleus, even if stellar feedback is included (Fanali et al. 2015; Li et al. 2017; Tress et al. 2020). The last two columns illustrate the spatial distribution of the newly formed stars color-coded by their chemistries ([Fe/H] and [Mg/Fe]). Although we do not observe an inner gas bar in S2BSMU, newly formed stars inside the ring follow the shape and rotation of the stellar inner bar, similar to the cascade bar formation scenario proposed in previous studies (e.g., Shlosman et al. 1989, 1990; Hopkins & Quataert 2010). This bar-shaped, newly formed stellar structure is more metal-rich and

---

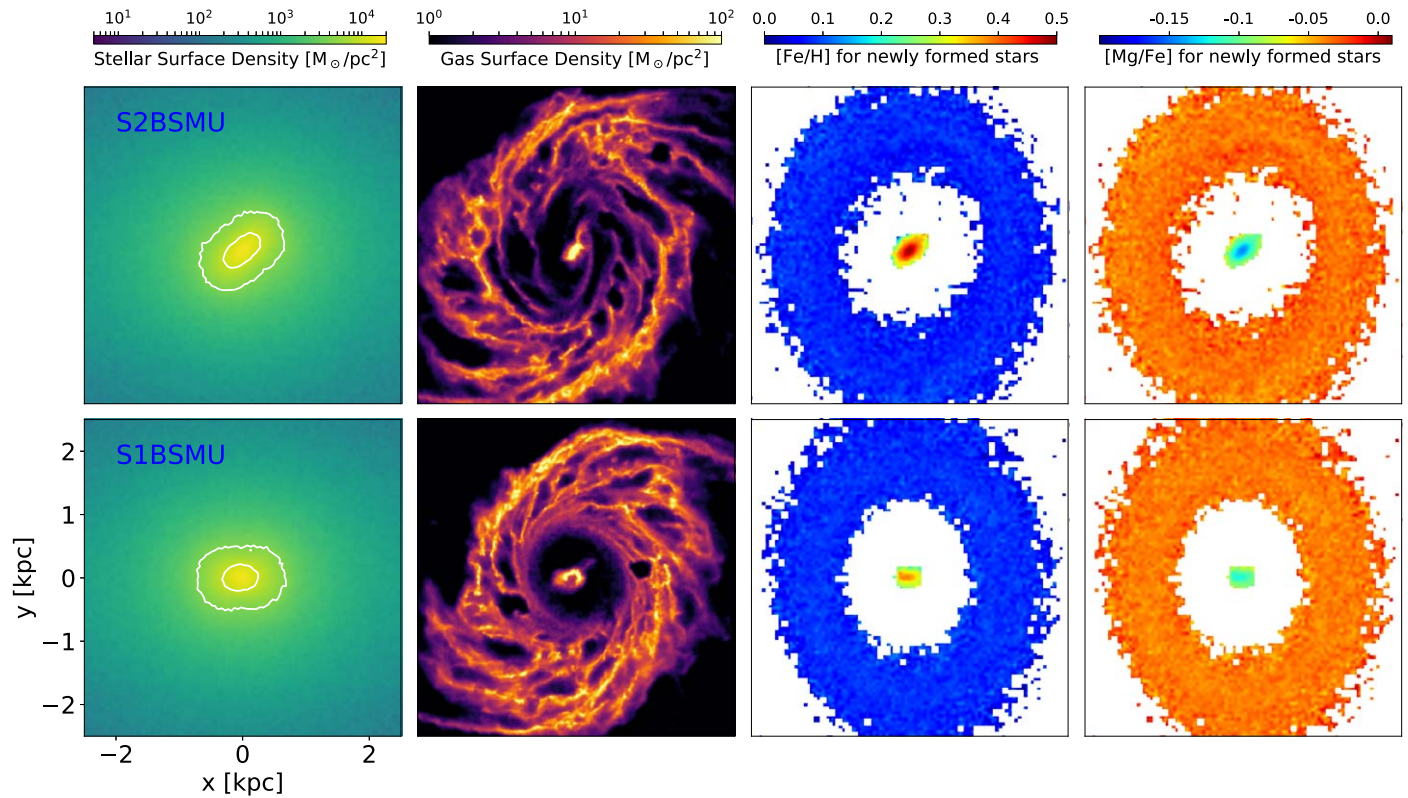[16] The faint gas blob at the center of S0BSMU is probably due to numerical diffusion.

Figure 7. Zoom-in view of Figure 6 to the central 2.5 kpc. The first and second columns are the stellar and gas surface densities. The third and fourth columns plot the metallicity (represented by [Fe/H]) and α abundance (represented by [Mg/Fe]) of the newly formed stars.

less α-enhanced compared to the surroundings, consistent with the observations of the inner bar in NGC 5850 (de Lorenzo-Cáceres et al. 2019b). The newly formed stars in S1BSMU show a similar pattern, but not as strongly as in S2BSMU.

In Figure 8, we plot the enclosed mass, mass inflow rate, and SFR for these three models at R_{outer} (left column) and R_{inner} (right column). The accumulated masses at R_{outer} are almost identical for S2BSMU and S1BSMU, but the two models diverge inside R_{inner}. The inner bar in S2BSMU drives ∼three times more mass inside R_{inner} compared with the SB model. The mass inflow rate of S2BSMU at R_{inner} is quasiperiodic and related to the inner bar dynamics, as shown in Figure 5. By contrast, the mass inflow rate of S1BSMU at R_{inner} is mostly dominated by stellar feedback, and the periodicity disappears. We obtained a time-averaged mass inflow rate of $0.144\,M_{\odot}\,\mathrm{yr}^{-1}$ at R_{outer} and $0.013\,M_{\odot}\,\mathrm{yr}^{-1}$ at R_{inner} for S1BSMU within the time interval of $t = 0.6$–1.6 Gyr; the ratio of these two inflow rates is ∼10.8, similar to the results in Tress et al. (2020). Model S2BSMU increases the central inflow rate to $0.044\,M_{\odot}\,\mathrm{yr}^{-1}$, reducing the ratio to ∼3.4. The control model S0BSMU has weak inflows (probably caused by diffusion and numerical effects), which are negligible compared with the other two models. We therefore conclude that the inner bar in S2Bs indeed helps gas flowing inward.

In addition, we find that S2BSMU has the highest SFR in both regions, as shown in the fourth row of Figure 8. This is expected as a consequence of more accumulated gas in the center. Observations have shown that bars can enhance central star formation (e.g., Lin et al. 2017, 2020), and our results imply that multiple bars may further amplify this effect. In fact, the total SFR in S2BSMU is larger than that in the other two models during most of the time in our simulations (solid lines

in Figure 9). This indicates that bars may not significantly reduce the SFR within a short period in our gas-poor models (but see also Khoperskov et al. 2018). The SFR in S2BSMU and S1BSMU at $R > R_{\mathrm{outer}}$ is slightly lower than that in S0BSMU (dashed lines in Figure 9). This is probably due to a smaller gas surface density in the outer disk region, as a significant fraction of gas has been driven inside R_{outer}.

3.2.2. Kennicutt–Schmidt Relation

We also investigate the molecular Kennicutt–Schmidt (KS) relation (Schmidt 1959; Kennicutt 1998) that connects the molecular gas surface density (Σ_{mol}) to the SFR surface density (Σ_{SFR}) in our models. Motivated by Querejeta et al. (2021), who used PHANGS-ALMA data (Leroy et al. 2021) to explore the KS relation in different galactic environments, we dissect our simulations into ∼1.3 kpc wide hexagonal bins.[17] The gas and SFR surface densities are then estimated inside each bin and plotted as colored dots in Figure 10. We divided the bins into three groups based on their radius: inside the inner bar (orange), outside the inner bar but roughly covering the nuclear ring (blue), and the disk region (gray). In general, the KS relation in our model is similar to the global fit in Querejeta et al. (2021; black dashed line), which implies a weak environmental (or radial) dependence of the star formation efficiency. Centers (orange points) in barred models (S2BSMU and S1BSMU) have shorter depletion times than the rest of the disk, also consistent with the findings in Querejeta et al. (2021). In addition, the depletion time in the center of S2BSMU seems to be even smaller than that in S1BSMU.

---

[17] See the inset in the middle panel of Figure 10, which is similar to Figure 3 in Querejeta et al. (2021).
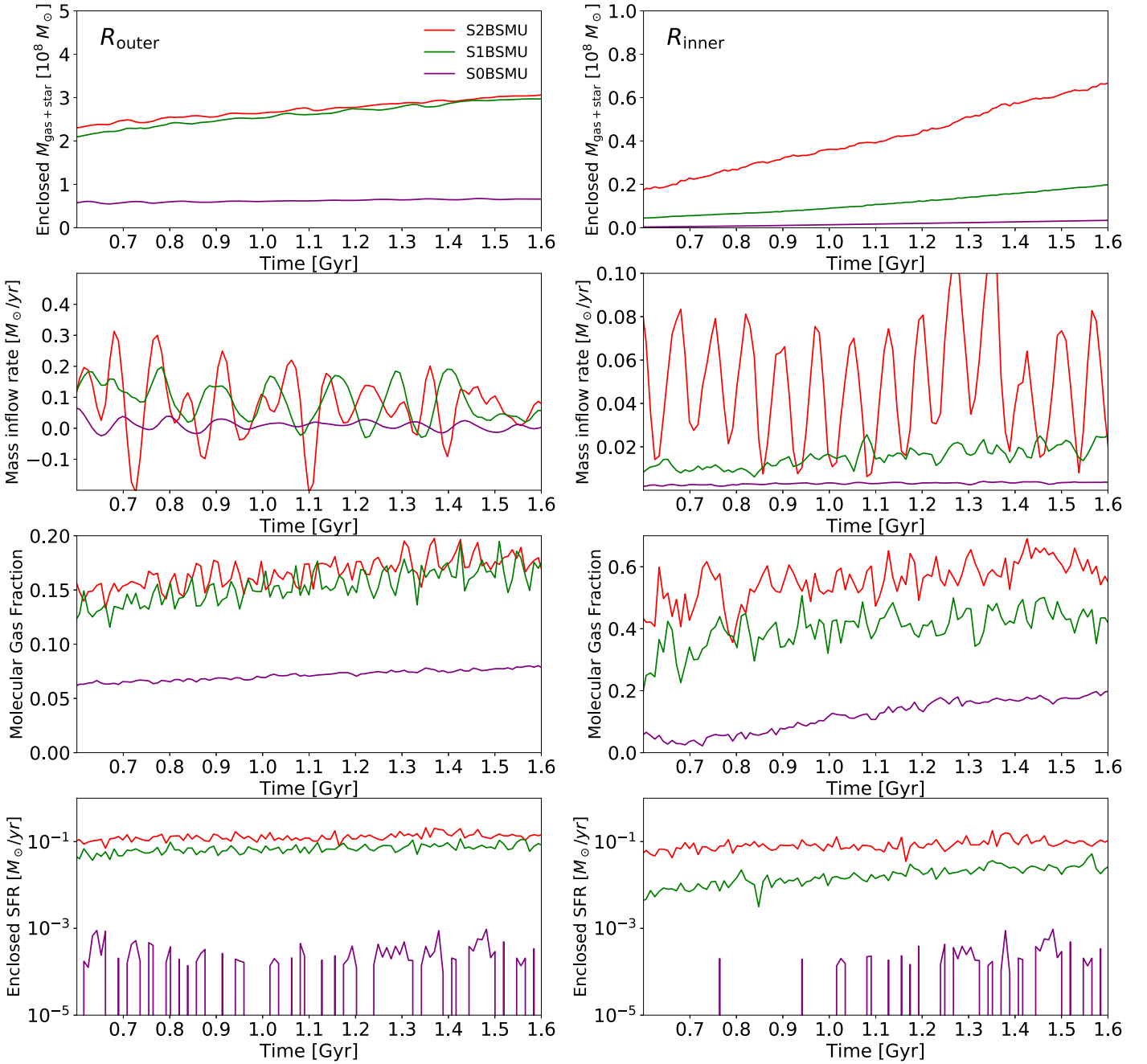
Figure 8. Comparison of the enclosed mass (first row), mass inflow rate (second row), molecular gas fraction (third row), and SFR (fourth row) at two characteristic radii ($R_{\rm outer} = 3.75$ and $R_{\rm inner} = 0.75$ kpc) of models S2BSMU, S1BSMU, and S0BSMU. The molecular gas fraction is defined as the ratio of the molecular and total gas mass. Note that the range of the y-axis is not the same in the left and right columns.

This is possibly due to a higher molecular gas fraction in the central regions of S2BSMU, as shown in the third row of Figure 8. On the other hand, the low gas surface density and SFR in the center of the unbarred model S0BSMU are simply due to our centrally-holed initial gas disk setup and thus cannot reflect the real central environments in unbarred galaxies. We therefore conclude that the SMUGGLE model can reproduce the latest observations reasonably well. In the SMUGGLE model, we adopt a constant star formation efficiency per freefall time ($\epsilon_{\rm sf} = 0.01$) and compute the SFR based on the molecular gas only; the KS relation is then captured by the self-regulated star formation and feedback processes. However, there are hints that $\epsilon_{\rm sf}$ may vary systematically with $\Sigma_{\rm mol}$ and $\Sigma_{\rm SFR}$ (Sun et al. 2023). We leave a detailed comparison of the

star formation laws between simulations and observations for future studies.

3.3. Long-term Evolution

Figure 5 shows that the inner bar in S2BSMU gradually decays due to accumulated central mass. We therefore use S2BEXP to test how long the inner bar will survive if there is an even higher gas mass at the center from the beginning. The gas mass inside $R_{\rm inner}$ is ~0.1% stellar mass at $t = 0$ for this model, which meets the inner bar dissolution criterion in Du et al. (2017). The evolution of the Fourier component A_2/A_0 and inner bar pattern speed is shown in Figure 11. We find that the independent pattern speed inside $R_{\rm inner}$ disappears at
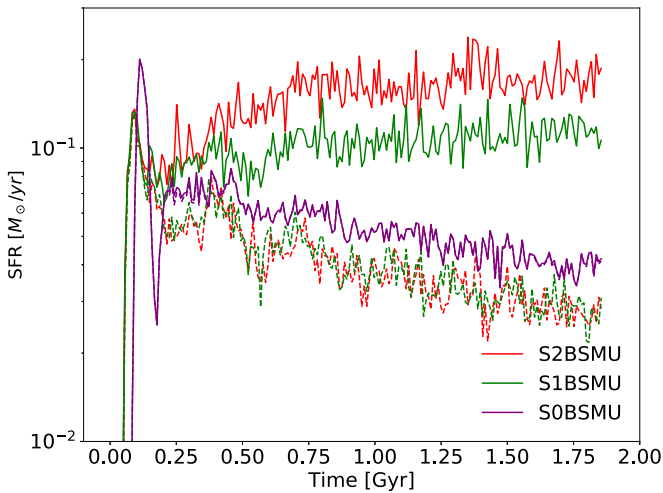
Figure 9. Solid lines: total SFR as a function of time in S2BSMU, S1BSMU, and S0BSMU. Dashed lines: SFR at $R \geqslant R_{\mathrm{outer}} = 3.75$ kpc as a function of time in the models.

$t \sim 2$ Gyr. At this moment, the contours of the stellar surface density in the central 1 kpc are nearly round (see the third column of Figure 12). We conclude that the inner bar fully dissolves at $t \sim 2$ Gyr in S2BEXP. The second and third columns of Figure 12 are two snapshots before and after the dissolution of the inner bar. We note that the outer bar also weakens considerably in this model.

We plot the evolution of 2D stellar kinematic maps of S2BEXP in Figure 12. The top and bottom rows show the second (σ) and fourth (h_4) Gauss–Hermite moments (Gerhard 1993; van der Marel & Franx 1993) of the vertical velocity (v_z) distribution. We include both the old stars and the newly formed stars in this figure. The σ-humps (de Lorenzo-Cáceres et al. 2008; Du et al. 2016) along the minor axis of the inner bar are clearly seen in the first column, but this feature disappears when the inner bar has been fully destroyed. The central region then remains roughly axisymmetric until the end of the simulation (see also Figure 8 in Guo et al. 2020). The h_4 maps reveal a ringlike structure and central blob that peak better after $t \sim 1.7$ Gyr and are possibly associated with the newly formed stars in the simulation. Even though the star formation is high in the inner bar region, the newly formed stars mainly follow chaotic orbits scattered by the CMC and can hardly support the inner bar structure as suggested by Nakatsuno & Baba (2023). Strong stellar feedback of young stars may also partially contribute to the dissolution of the inner bar, as it prevents star-forming clouds from settling on the inner bar supporting orbits (see also Section 3.1.1 and Figure 13). These kinematic signatures could be potentially useful for detecting dissolved inner bars in future integral field unit observations.

4. Comparison with Observations

Inflow signatures related to the inner bar have been reported in observations (e.g., Fathi et al. 2006; Schinnerer et al. 2006, 2007; González-Alfonso et al. 2021). Based on the recent PHANGS-ALMA data, we find six S2B candidates (NGC 1068, NGC 1087, NGC 1317, NGC 1433, NGC 4304, and NGC 4321) according to the classifications in Erwin (2004) and Buta et al. (2015). Object NGC 1433 probably has the most similar bar shapes (i.e., stellar surface density contours) compared to our S2BSMU model. Although our S2BSMU

model is not designed to match any particular galaxy, we still compare it with NGC 1433 in Figure 13. The top row shows the S^4G 3.6 μm image, CO(2–1) integrated intensity map, CO intensity-weighted mean line-of-sight (LOS) velocity map, and residual velocity map obtained by subtracting the circular motion (i.e., the spider diagram) from the V_{los} map of NGC 1433. The first two CO maps are the same as in the PHANGS-ALMA survey paper (moment 0 and 1 maps in Leroy et al. 2021). The circular velocity curve used to derive the residual velocity map is from Lang et al. (2020; see their Equation (10) and Table 4, with $V_0 = 204.5$ km s^{-1} and $R_t = 0.59$ kpc). The middle and bottom rows show the projected stellar surface density map, projected molecular gas surface density map, molecular gas LOS velocity map, and residual velocity map in S2BSMU at $t = 818$ and 892 Myr. These plots are obtained by projecting the stellar and molecular gas disk in the simulation with an inclination of 28°.6 and a disk position angle of 199°.7 (Buta et al. 2001; Lang et al. 2020). The circular velocity curve is derived by `DiskFit` (Sellwood & Spekkens 2015), which applies the tilted ring method[18] to the molecular gas V_{los} field ($V_0 = 270.0$ km s^{-1} and $R_t = 0.30$ kpc). We assume purely circular motion and do not consider radial or bisymmetric flows during the fitting, similar to Lang et al. (2020).

In Figure 13, the two snapshots of S2BSMU have similar bar orientations as in the S^4G image (first column). In the second column, multiple gas streams extending from the nuclear ring to the central part are seen both in the observation and in our model. This indicates a strong gas inflow that is also evident in the other five observed S2Bs. The presence of clumpy gas features around the nuclear ring suggests that these regions are undergoing intense star formation. The V_{los} maps in the third column also match qualitatively. Note that here we show the velocity information in the whole region of the simulation, which presents a larger view of the gas flows. We argue that reproducing exactly the observed CO V_{los} map of S2Bs would be quite challenging, since the effects of (stochastic) stellar feedback on the gas morphology and kinematics are as important as the gravitational effect of the inner bar (Section 3.1.1). We also demonstrated this in the middle and bottom rows of Figure 13; the stellar surface densities are almost identical at $t = 818$ and 892 Myr, but the gas morphology and V_{los} maps have a relatively large difference. In the fourth column, we show the residual velocity maps of the observation and simulation. The residual velocity map in the simulation looks more chaotic, possibly also due to strong stellar feedback. We note that the structures in the residual velocity map somewhat rely on whether one can measure the inclination and position angle of the disks accurately (e.g., Kolcu et al. 2023); thus, a large uncertainty may exist to make a reasonable comparison.

Another way to compare our model with real S2Bs is to calculate the mass inflow rate at different radii. We predict that the ratio of the mass inflow rate from the outer bar to the nuclear ring and from the nuclear ring to the center is around 3.4 for S2Bs, while this number increases to $\gtrsim 10$ for SB galaxies (Section 3.2). Wu et al. (2021) obtained a mass inflow rate of 12 $M_\odot$ yr^{-1} along the dust lanes of the outer bar in the S2B galaxy NGC 3504 based on ALMA CO data. It would be

---

[18] The tilted ring method may fail to extract the true circular velocity curve when bar-induced noncircular motions dominate the LOS velocity field. A more detailed analysis will be presented in J. Liu et al. (2023, in preparation).
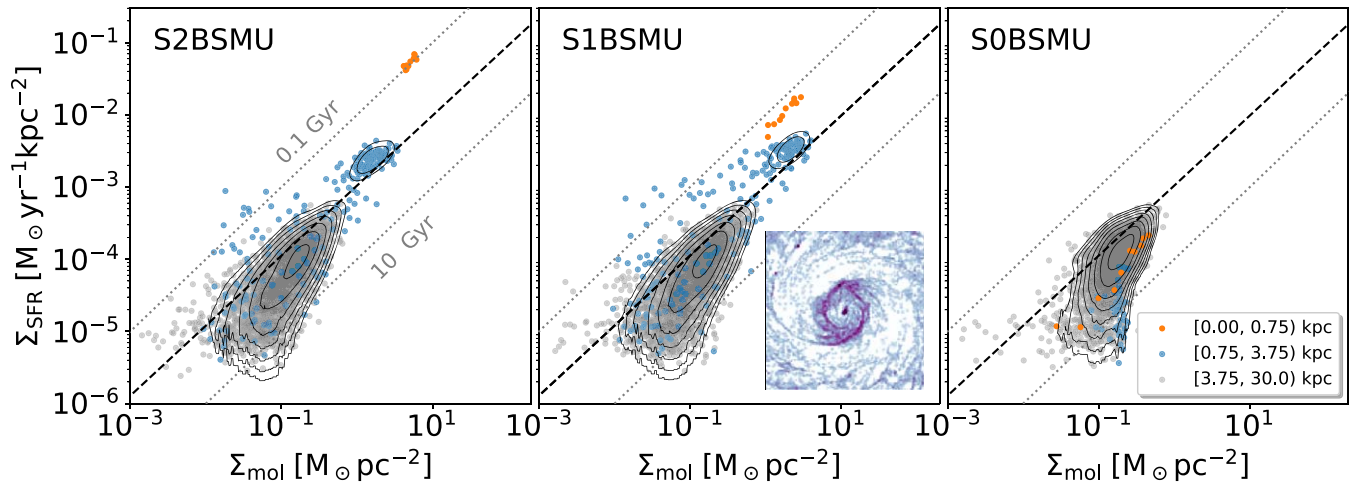
Figure 10. The KS relation in models S2BSMU, S1BSMU, and S0BSMU. Solid black curves are the contours of the scatter points. Only gas and newly formed stars in the disk region ($|z| \leqslant 2$ kpc) are considered in this plot. For each model, we include 11 snapshots separated by $\sim$100 Myr to increase the sample size. The black dashed line is the global fit from Querejeta et al. (2021) with a slope of 0.97. Two black dotted lines representing depletion times of 0.1 and 10 Gyr are included for comparison. The inset in the middle panel illustrates the placement of the hexagonal bins in our models. The bins are colored according to their galactocentric radius, and the underlying plot is the same gas surface density plot of S2BSMU shown in Figure 7.
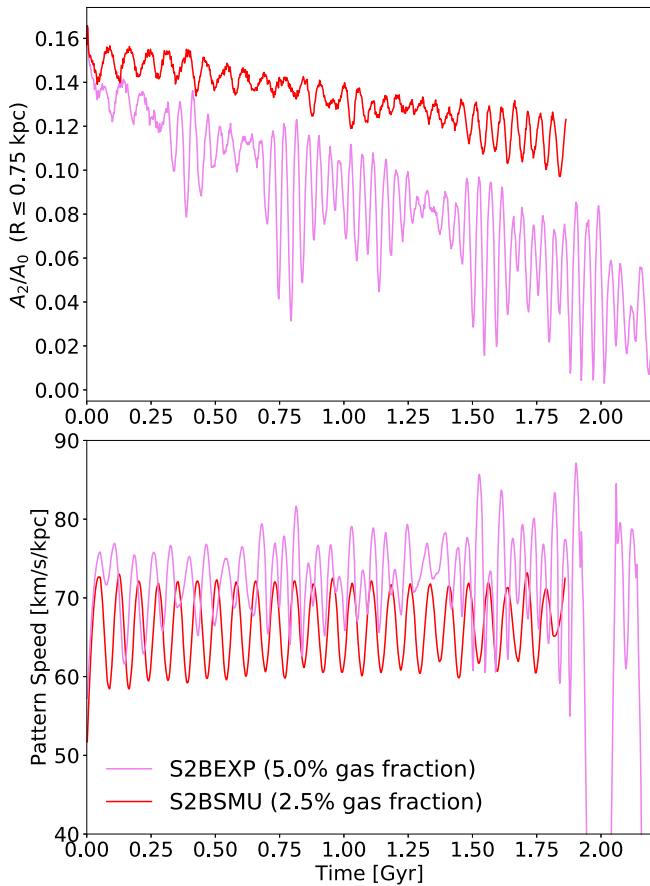
Figure 11. Evolution of A_2/A_0 (top) and pattern speed (bottom) in the inner bar region ($R \leqslant 0.75$ kpc) of two models with different gas fractions. At $t \gtrsim 1.7$ Gyr in S2BEXP, the pattern speed calculated using the A_2 phase angle time derivatives may be less accurate due to the small A_2 amplitude.

interesting to measure the radial motions of gas in this galaxy (as well as other S2Bs) at different radii and compare the results with SB galaxies (e.g., similar to Haan et al. 2009). However, this requires a detailed analysis of the observational data, which is the subject of future work.

5. Discussion

5.1. Comparison with Previous S2B Models

Our models suggest that inner bars are efficient at driving gas inflows, which does not support the previous S2B simulations in Maciejewski et al. (2002) and Rautiainen et al. (2002). We first note that the results in Maciejewski et al. (2002) may suffer from a now-recognized bug in the code CHMOG (see Kim et al. 2012). Indeed, Namekata et al. (2009) adopted a similar analytical S2B potential but a different nuclear bulge component compared with Maciejewski et al. (2002) and found significant inflows caused by the inner bar. The authors speculated that the shallow central potential in Maciejewski et al. (2002) may be the reason for the lack of inflow. While the model of Rautiainen et al. (2002) consisted of a live S2B model, its resolution may have been too low to resolve the central gas behavior, since it employed only 40,000 sticky gas particles within a 4.5 kpc radius gas disk. Thus, it is possible that the absence of strong gas inflows in Maciejewski et al. (2002) and Rautiainen et al. (2002) may be mostly attributed to numerical issues.

The inflow due to the inner bar is quasiperiodic in our S2B models. Shlosman & Heller (2002) and Namekata et al. (2009) found a similar cyclic inflow in their S2B simulations, although the pattern speeds and the shapes of the bars in their models are constant with time. This may imply that a pulsating inner bar is not necessary to produce a periodic inflow. The periodicity is likely due to the fact that the inner bar sweeps gas more efficiently (or shocks are more easily formed) when the two bars tend to be perpendicular with each other; i.e., a pattern speed difference for the two bars would be sufficient. We also find that the inner bar in our S2BEXP model does not revive after dissolution, which appears to differ from Wozniak (2015), who also included star formation and stellar feedback. This may imply that star formation is not the only key parameter for generating a recurrent inner bar or that the gas fraction is still too low in our models. It could also be due to the different implementations of the subgrid physics in the two studies.
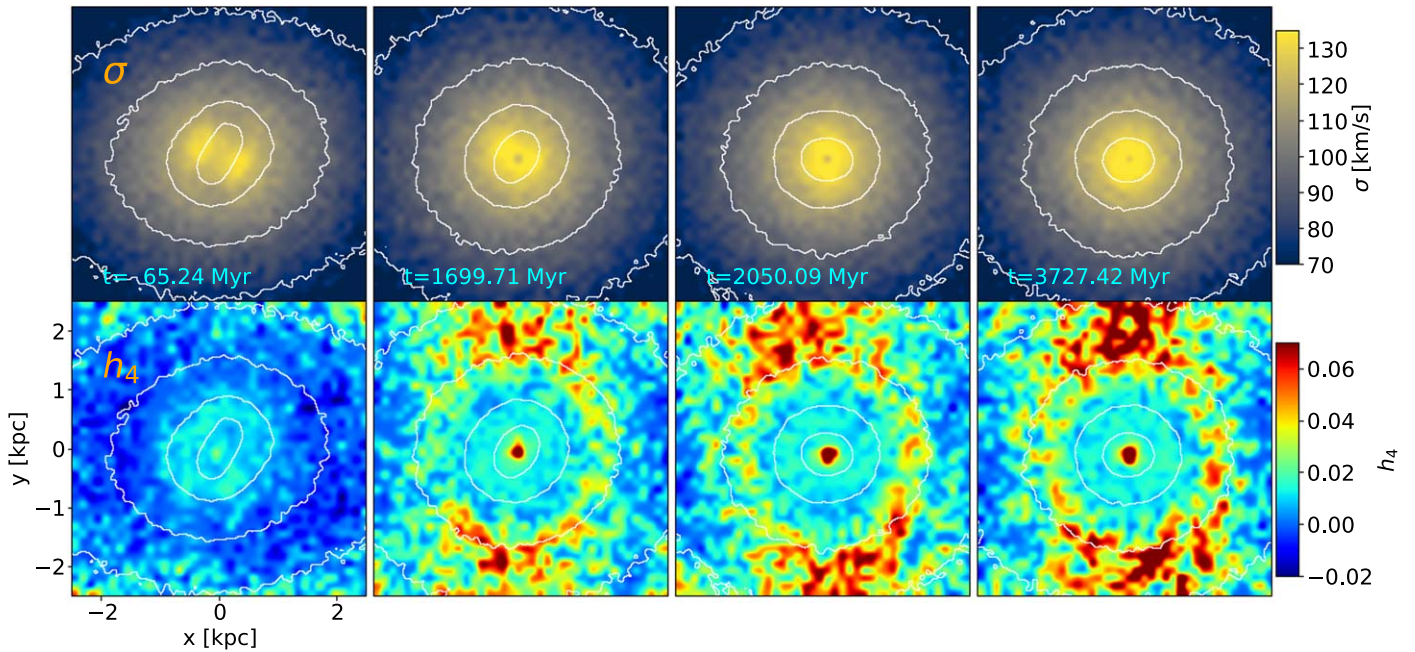
Figure 12. Kinematic maps of S2BEXP, viewed face-on. From left to right are four different epochs. The second (σ) and fourth (h_4) Gauss–Hermite moments of the vertical velocity v_z distribution are shown in the top and bottom rows, respectively. White lines represent the contours of the stellar surface density. The outer bar is aligned with the x-axis.

5.2. For How Long Does the Inner Bar Promote Gas Inflows?

According to the S2BEXP model, the inner bar is fully dissolved within $\sim$2 Gyr with a gas disk of $\sim$5% stellar mass. The gas inflow then stalls at the nuclear ring, similar to the case in S1BSMU. This timescale is longer than that obtained in Du et al. (2017; $\lesssim$1 Gyr), probably because the central potential of the CMC is "softer" than a nearly Keplerian one used in Du et al. (2017).

One important aspect that is not considered in our study is the feedback due to the active galactic nucleus (AGN). The huge energy released by the central engine may help to clear the accumulated gas at the center. The inner bar is then expected to be more robust against gas inflows than what we have found here. It is therefore reasonable to suggest that the inner bar can promote central gas inflows on a timescale of a few gigayears, although the inflows may be episodic. On the other hand, Irodotou et al. (2022) suggested that there is an anticorrelation between AGN feedback and bar strength in cosmological simulations; i.e., bars tend to be stronger and shorter if AGN feedback is not included. Future studies of the relation between AGN feedback and bar stability would be very useful to better understand this issue.

5.3. Do We Expect a Clear Correlation between S2Bs and AGNs?

In our S2B model, gas is funneled close to the Bondi radius (a few tens of parsecs) if a $1.0 \times 10^8\,M_\odot$ SMBH (Schwarzschild radius: $R_S = 9.57 \times 10^{-6}$ pc; Eddington accretion rate: $\dot{M}_{\mathrm{Edd}} = 2.2\,M_\odot\,\mathrm{yr}^{-1}$) has been present at the galactic center. The accretion flows around an SMBH are generally classified into the radiative mode, also known as quasar mode, which operates when the SMBH has high accretion rates, and the kinetic mode, also known as radio mode, which is typically important when the SMBH has low accretion rates. The boundary between the two modes is usually $\sim 2\%\dot{M}_{\mathrm{Edd}} = 0.043\,M_\odot\,\mathrm{yr}^{-1}$ (summarized

in Yuan et al. 2020). Our fiducial S2B model with a lightweight gaseous disk has the same order of gas inflow rate, and this level of fueling can be easily achieved in local disk galaxies that host quasars (Zhao et al. 2019). If the SMBHs in S2Bs are in quasar mode, the timescale for the gas to flow from the accretion disk ($R = 1000R_S \approx 0.01$ pc) to feed the SMBH is 0.44 Gyr based on Equation (6) of Yuan et al. (2018). With an additional freefall timescale (a few tens of megayears) for gas to flow into the accretion disk from the Bondi radius, the overall timescale of gas inflows from the Bondi radius to feed the central SMBH can be estimated at a few hundred megayears, which is longer than the rotation period of the inner bar in our model. Though gas inflows are more prominent when the inner bar is perpendicular to its outer counterpart, it is not likely to result in a clear correlation between the relative orientation of the two bars and any AGN activity.

Do we expect to find a higher frequency of AGNs in S2B galaxies? Our simulations suggest that SMBHs may grow rapidly when an inner bar exists. About $10^7\,M_\odot$ of gas accumulates in the central 100 pc of S2BSMU within 0.5 Gyr even with a rather lightweight initial gaseous disk. As suggested in Du et al. (2017) and Guo et al. (2020), as well as the results of this paper, the inner bar will be destroyed once enough gas accumulates in the galaxy center, no matter whether the gas has fallen into the SMBH. The inner bar may be in the process of dissolution, considering the potential delay of AGN activity by around a few hundred megayears estimated above. We also note that any possible link between S2Bs and AGNs may disappear if the first inner bar that powers the AGN decays and a new one forms at later times, similar to the scenario proposed for large-scale bars (e.g., Sellwood & Moore 1999; Li et al. 2017). It is therefore understandable that no clear relation between inner bars and AGNs is reported in observations (Laine et al. 2002; Erwin & Sparke 2002; Erwin 2011). On the other hand, recent studies seem to suggest that AGNs are preferentially found in barred galaxies (Alonso et al.
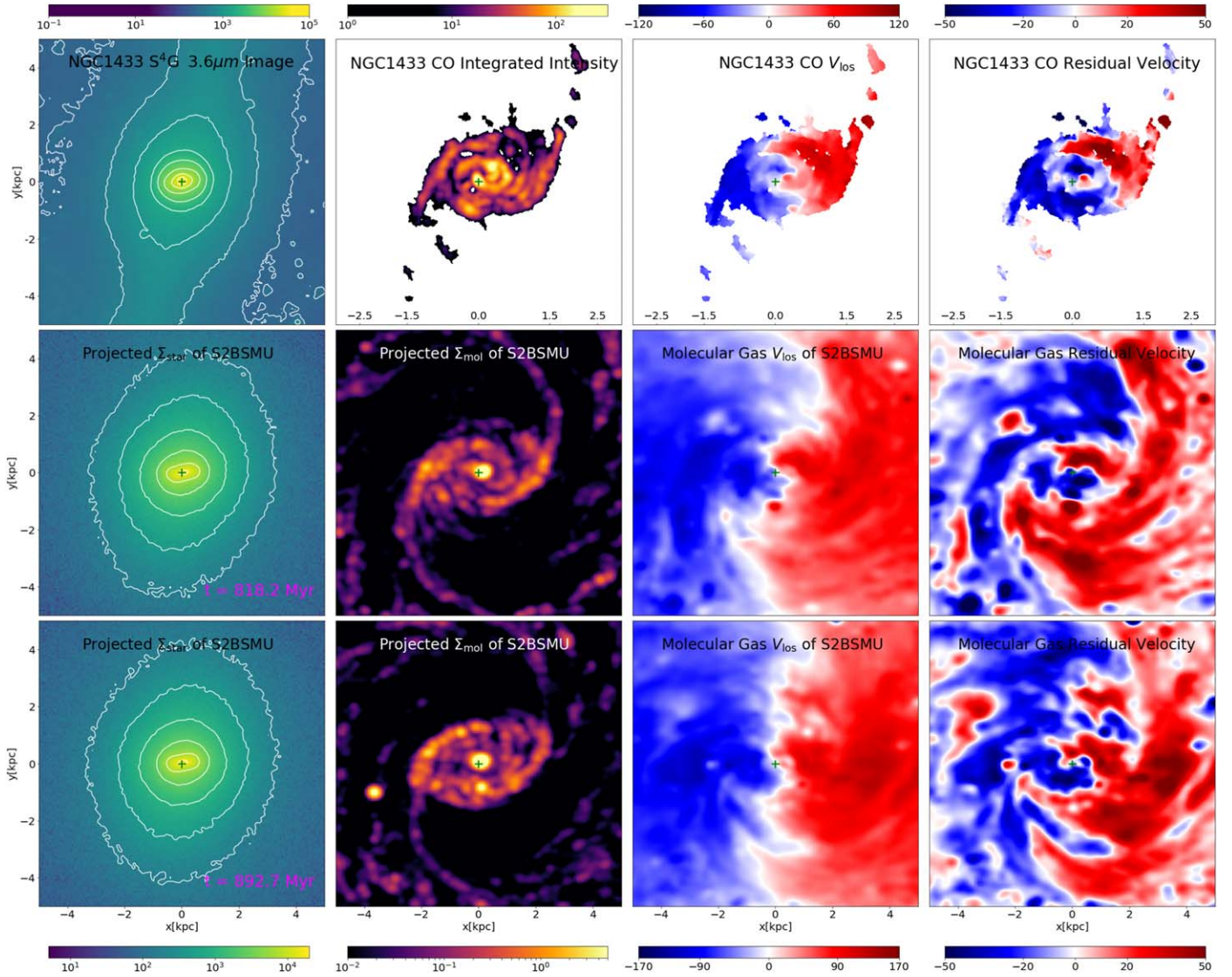
Figure 13. Comparison between an observed S2B galaxy, NGC 1433, and our S2BSMU model. We adopt a distance of 18.63 Mpc, a systemic velocity of 1057.4 km s^{-1}, a disk position angle of 199°7, and an inclination angle of 28°6 for this galaxy (Buta et al. 2001; Lang et al. 2020). Top row, left to right: S^{4}G 3.6 μm image (unit: $L_\odot$ pc^{-2}), PHANGS-ALMA CO(2–1) integrated intensity map (moment 0; unit: K km s^{-1}), intensity-weighted mean velocity map (moment 1; unit: km s^{-1}), and residual velocity map obtained by subtracting circular motions (unit: km s^{-1}). Note that the spatial scales are different for the S^{4}G image and ALMA maps. Middle row, left to right: projected stellar surface density map (unit: $M_\odot$ pc^{-2}), projected molecular gas surface density map (unit: $M_\odot$ pc^{-2}), molecular gas LOS velocity map (unit: km s^{-1}), and molecular gas residual velocity map (unit: km s^{-1}) for the model at $t = 818.2$ Myr. Bottom row: same as the second row but at $t = 892.7$ Myr. The green plus sign marks the center of the image ($x = 0$, $y = 0$).

2018; Silva-Lima et al. 2022), although the S2B fraction in the samples remains unclear.

5.4. Are Inner Bars Long-lived or Recurrent?

The high frequency of observed S2Bs (Erwin 2011) indicates that inner bars are either long-lived or easily reformed after dissolution. De Lorenzo-Cáceres et al. (2019a) performed a detailed photometric analysis of 17 nearby S2Bs and found that most bulges in their sample have an intermediate Sérsic index ($n \approx 2$) and lie at the top sequence of the Kormendy relation (Kormendy 1977); i.e., they are similar to classical bulges. On the other hand, the simulation of Guo et al. (2020) shows that the remnant of the dissolved inner bar shares such properties with those of observed bulges in S2Bs. This makes one wonder if the inner bar in S2Bs can reform after dissolution instead of being a long-lived structure. If the inner bars have

dissolved and reformed over time, we should see these classical bulges as relics in observed S2Bs, which seems to be consistent with de Lorenzo-Cáceres et al. (2019a). However, since there are multiple ways to form classical bulges, this does not necessarily mean that inner bars have to be recurrent. It is possible that two kinds of inner bars exist in the Universe, as de Lorenzo-Cáceres et al. (2020) found that there are two distinct groups of inner bars in terms of their in-plane length and ellipticity. Whether the properties of long-lived inner bars are systematically different from those of recurrent ones needs further investigation.

6. Summary

In this study, we have used high-resolution numerical simulations to explore gas flow patterns in a galaxy with two independently rotating bars (S2Bs). Different gas physics

setups are tested, and the gravitational effect of the inner bar is highlighted with control models. Our main findings are summarized as follows.

(1) We find that the inner bar can drive gas flow inward. The inflow is periodic, and it is stronger when the two bars are perpendicular with respect to each other, possibly due to clearer shocks in the inner bar at this orientation (Figure 5). The time-averaged central inflow rate in our S2B model is about three times higher than that in the single-barred one (Figure 8).

(2) Gas forms multiple streams down to the center from the nuclear ring in our S2B model, while this is not observed in the single-barred simulation (Figure 7). Outside the nuclear ring, the flow patterns are very similar between single- and double-barred galaxies. A gas inner bar is formed in the S2B model without stellar feedback, but it is erased when feedback is included (Figure 6). The gas flow pattern in our S2B model with SMUGGLE enabled is qualitatively consistent with a few observed S2Bs (Figure 13).

(3) The S2B model has the highest star formation rate compared with the single- and nonbarred models (Figure 9) at a given stellar mass. This may be explained by a higher star formation efficiency (or shorter depletion time), together with a higher accumulated gas mass in the center of the S2B model. We also find that the depletion time in the central region is shorter than that in the disk, similar to recent observations (Figure 10).

Acknowledgments

ORCID iDs

Zhi Li ⓘ https://orcid.org/0000-0002-0627-8009
Min Du ⓘ https://orcid.org/0000-0001-9953-0359
Victor P. Debattista ⓘ https://orcid.org/0000-0001-7902-0116
Juntai Shen ⓘ https://orcid.org/0000-0001-5604-1643
Hui Li ⓘ https://orcid.org/0000-0002-1253-2763
Jie Liu ⓘ https://orcid.org/0000-0003-4052-8785
Mark Vogelsberger ⓘ https://orcid.org/0000-0001-8593-7692
Angus Beane ⓘ https://orcid.org/0000-0002-8658-1453
Federico Marinacci ⓘ https://orcid.org/0000-0003-3816-7028
Laura V. Sales ⓘ https://orcid.org/0000-0002-3790-720X

References

Alonso, S., Coldwell, G., Duplancic, F., Mesa, V., & Lambas, D. G. 2018, A&A, 618, A149
Asplund, M., Grevesse, N., Sauval, A. J., & Scott, P. 2009, ARA&A, 47, 481
Athanassoula, E. 1992, MNRAS, 259, 345
Athanassoula, E. 2003, MNRAS, 341, 1179
Beane, A., Hernquist, L., D'Onghia, E., et al. 2023, ApJ, 953, 173
Bittner, A., de Lorenzo-Cáceres, A., Gadotti, D. A., et al. 2021, A&A, 646, A42
Brown, J. S., Valluri, M., Shen, J., & Debattista, V. P. 2013, ApJ, 778, 151
Burger, J. D., Zavala, J., Sales, L. V., et al. 2022, MNRAS, 513, 3458
Buta, R., & Block, D. L. 2001, ApJ, 550, 243
Buta, R., & Crocker, D. A. 1993, AJ, 105, 1344
Buta, R., Ryder, S. D., Madsen, G. J., et al. 2001, AJ, 121, 225
Buta, R. J., Sheth, K., Athanassoula, E., et al. 2015, ApJS, 217, 32
de Lorenzo-Cáceres, A., Falcón-Barroso, J., Vazdekis, A., & Martínez-Valpuesta, I. 2008, ApJL, 684, L83
de Lorenzo-Cáceres, A., Méndez-Abreu, J., Thorne, B., & Costantin, L. 2019a, MNRAS, 484, 665
de Lorenzo-Cáceres, A., Méndez-Abreu, J., Thorne, B., & Costantin, L. 2020, MNRAS, 494, 1826
de Lorenzo-Cáceres, A., Sánchez-Blázquez, P., Méndez-Abreu, J., et al. 2019b, MNRAS, 484, 5296
Debattista, V. P., & Shen, J. 2007, ApJL, 654, L127
Du, M., Debattista, V. P., Shen, J., & Cappellari, M. 2016, ApJ, 828, 14
Du, M., Debattista, V. P., Shen, J., Ho, L. C., & Erwin, P. 2017, ApJL, 844, L15
Du, M., Shen, J., & Debattista, V. P. 2015, ApJ, 804, 139
Englmaier, P., & Gerhard, O. 1997, MNRAS, 287, 57
Erwin, P. 2004, A&A, 415, 941
Erwin, P. 2005, MNRAS, 364, 283
Erwin, P. 2011, MSAIS, 18, 145
Erwin, P., & Sparke, L. S. 2002, AJ, 124, 65
Fanali, R., Dotti, M., Fiacconi, D., & Haardt, F. 2015, MNRAS, 454, 3641
Fathi, K., Storchi-Bergmann, T., Riffel, R. A., et al. 2006, ApJL, 641, L25
Fragkoudi, F., Athanassoula, E., & Bosma, A. 2017, MNRAS, 466, 474
Friedli, D., & Martinet, L. 1993, A&A, 277, 27
Gerhard, O. E. 1993, MNRAS, 265, 213
González-Alfonso, E., Pereira-Santaella, M., Fischer, J., et al. 2021, A&A, 645, A49
Guo, M., Du, M., Ho, L. C., Debattista, V. P., & Zhao, D. 2020, ApJ, 888, 65
Haan, S., Schinnerer, E., Emsellem, E., et al. 2009, ApJ, 692, 1623
Harris, C. R., Millman, K. J., van der Walt, S. J., et al. 2020, Natur, 585, 357
Heller, C. H., Shlosman, I., & Athanassoula, E. 2007, ApJL, 657, L65
Hopkins, P. F., & Quataert, E. 2010, MNRAS, 407, 1529
Hunter, J. D. 2007, CSE, 9, 90
Irodotou, D., Fragkoudi, F., Pakmor, R., et al. 2022, MNRAS, 513, 3768
Kennicutt, R. C. J. 1998, ApJ, 498, 541
Khoperskov, S., Haywood, M., Di Matteo, P., Lehnert, M. D., & Combes, F. 2018, A&A, 609, A60
Kim, W. T., Seo, W. Y., Stone, J. M., Yoon, D., & Teuben, P. J. 2012, ApJ, 747, 60
Kluyver, T., Ragan-Kelley, B., Pérez, F., et al. 2016, in Positioning and Power in Academic Publishing: Players, Agents and Agendas, ed. F. Loizides & B. Schmidt (Amsterdam: IOS Press), 87
Kolcu, T., Maciejewski, W., Gadotti, D. A., et al. 2023, MNRAS, 524, 207
Kormendy, J. 1977, ApJ, 218, 333
Laine, S., Shlosman, I., Knapen, J. H., & Peletier, R. F. 2002, ApJ, 567, 97
Lang, P., Meidt, S. E., Rosolowsky, E., et al. 2020, ApJ, 897, 122
Leroy, A. K., Hughes, A., Liu, D., et al. 2021, ApJS, 255, 19
Li, H., Vogelsberger, M., Bryan, G. L., et al. 2022, MNRAS, 514, 265
Li, Z., Sellwood, J. A., & Shen, J. 2017, ApJ, 850, 67
Li, Z., Shen, J., & Kim, W. T. 2015, ApJ, 806, 150
Li, Z. Y., Shen, J., Rich, R. M., Kunder, A., & Mao, S. 2014, ApJL, 785, L17
Lin, L., Li, C., Du, C., et al. 2020, MNRAS, 499, 1406
Lin, L., Li, C., He, Y., Xiao, T., & Wang, E. 2017, ApJ, 838, 105
Lin, L. H., Wang, H. H., Hsieh, P. Y., et al. 2013, ApJ, 771, 8
Maciejewski, W., & Sparke, L. S. 2000, MNRAS, 313, 745

Maciejewski, W., Teuben, P. J., Sparke, L. S., & Stone, J. M. 2002, MNRAS, 329, 502

Marinacci, F., Sales, L. V., Vogelsberger, M., Torrey, P., & Springel, V. 2019, MNRAS, 489, 4233

Méndez-Abreu, J., de Lorenzo-Cáceres, A., Gadotti, D. A., et al. 2019, MNRAS, 482, L118

Moon, S., Kim, W. T., Kim, C. G., & Ostriker, E. C. 2022, ApJ, 925, 99

Nakatsuno, N., & Baba, J. 2023, arXiv:2308.15029

Namekata, D., Habe, A., Matsui, H., & Saitoh, T. R. 2009, ApJ, 691, 1525

Querejeta, M., Schinnerer, E., Meidt, S., et al. 2021, A&A, 656, A133

Rautiainen, P., Salo, H., & Laurikainen, E. 2002, MNRAS, 337, 1233

Romeo, A. B., & Fathi, K. 2016, MNRAS, 460, 2360

Schinnerer, E., Böker, T., Emsellem, E., & Downes, D. 2007, A&A, 462, L27

Schinnerer, E., Böker, T., Emsellem, E., & Lisenfeld, U. 2006, ApJ, 649, 181

Schmidt, M. 1959, ApJ, 129, 243

Sellwood, J. A., & Moore, E. M. 1999, ApJ, 510, 125

Sellwood, J. A., & Spekkens, K. 2015, arXiv:1509.07120

Shen, J., & Debattista, V. P. 2009, ApJ, 690, 758

Shen, J., & Sellwood, J. A. 2004, ApJ, 604, 614

Shlosman, I. 2005, in AIP Conf. Ser. 783, The Evolution of Starbursts, ed. S. Hüttmeister et al. (Melville, NY: AIP), 223

Shlosman, I., Begelman, M. C., & Frank, J. 1990, Natur, 345, 679

Shlosman, I., Frank, J., & Begelman, M. C. 1989, Natur, 338, 45

Shlosman, I., & Heller, C. H. 2002, ApJ, 565, 921

Silva-Lima, L. A., Martins, L. P., Coelho, P. R. T., & Gadotti, D. A. 2022, A&A, 661, A105

Sivasankaran, A., Blecha, L., Torrey, P., et al. 2022, MNRAS, 517, 4752

Sormani, M. C., Binney, J., & Magorrian, J. 2015, MNRAS, 449, 2421

Springel, V. 2010, MNRAS, 401, 791

Springel, V., Di Matteo, T., & Hernquist, L. 2005, MNRAS, 361, 776

Sun, J., Leroy, A. K., Ostriker, E. C., et al. 2023, ApJL, 945, L19

Tacchella, S., Smith, A., Kannan, R., et al. 2022, MNRAS, 513, 2904

Tress, R. G., Sormani, M. C., Glover, S. C. O., et al. 2020, MNRAS, 499, 4455

van der Marel, R. P., & Franx, M. 1993, ApJ, 407, 525

Virtanen, P., Gommers, R., Oliphant, T. E., et al. 2020, NatMe, 17, 261

Vogelsberger, M., Genel, S., Sijacki, D., et al. 2013, MNRAS, 436, 3031

Wang, H. H., Klessen, R. S., Dullemond, C. P., van den Bosch, F. C., & Fuchs, B. 2010, MNRAS, 407, 705

Weinberger, R., Springel, V., & Pakmor, R. 2020, ApJS, 248, 32

Weiner, B. J., Sellwood, J. A., & Williams, T. B. 2001, ApJ, 546, 931

Wozniak, H. 2015, A&A, 575, A7

Wu, Y. T., Pfenniger, D., & Taam, R. E. 2016, ApJ, 830, 111

Wu, Y. T., Trejo, A., Espada, D., & Miyamoto, Y. 2021, MNRAS, 504, 3111

Yuan, F., Ostriker, J. P., Yoon, D., et al. 2020, in Proc. IAU 342, Perseus in Sicily: From Black Hole to Cluster Outskirts, ed. K. Asada et al. (Cambridge: Cambridge Univ. Press), 101

Yuan, F., Yoon, D., Li, Y. P., et al. 2018, ApJ, 857, 121

Zhao, D., Ho, L. C., Zhao, Y., Shangguan, J., & Kim, M. 2019, ApJ, 877, 52